

Modelling the probability of ionospheric irregularity occurrence over African low latitude region



Patrick Mungufeni^{a,*}, Edward Jurua^a, John Bosco Habarulema^{b,c}, Simon Anguma Katrini^a

^a Mbarara University of Science and Technology, Mbarara, Uganda

^b South African National Space Agency (SANSA) Space Science, 7200 Hermanus, South Africa

^c Department of Physics and Electronics, Rhodes University, 6140 Grahamstown, South Africa

ARTICLE INFO

Article history:

Received 3 December 2014

Received in revised form

17 February 2015

Accepted 23 March 2015

Available online 28 March 2015

Keywords:

Modelling

Ionospheric irregularities

Low-latitude ionosphere

ABSTRACT

This study presents models of geomagnetically quiet time probability of occurrence of ionospheric irregularities over the African low latitude region. GNSS-derived ionospheric total electron content data from Mbarara, Uganda (0.60°S, 30.74°E, geographic, 10.22°S, *magnetic*) and Libreville, Gabon (0.35°N, 9.68°E, geographic, 8.05°S, *magnetic*) during the period 2001–2012 were used. First, we established the rate of change of total electron content index (ROTI) value associated with background ionospheric irregularity over the region. This was done by analysing GNSS carrier-phases at L-band frequencies L1 and L2 with the aim of identifying cycle slip events associated with ionospheric irregularities. We identified at both stations a total of 699 events of cycle slips. The corresponding median ROTI value at the epochs of the cycle slip events was 0.54 TECU/min. The probability of occurrence of ionospheric irregularities associated with ROTI ≥ 0.5 TECU/min was then modelled by fitting cubic B-splines to the data. The aspects the model captured included diurnal, seasonal, and solar flux dependence patterns of the probability of occurrence of ionospheric irregularities. The model developed over Mbarara was validated with data over Mt. Baker, Uganda (0.35°N, 29.90°E, geographic, 9.25°S, *magnetic*), Kigali, Rwanda (1.94°S, 30.09°E, geographic, 11.62°S, *magnetic*), and Kampala, Uganda (0.34°N, 32.60°E, geographic, 9.29°S, *magnetic*). For the period validated at Mt. Baker (approximately, 137.64 km, north west), Kigali (approximately, 162.42 km, south west), and Kampala (approximately, 237.61 km, north east) the percentages of the number of errors (difference between the observed and the modelled probability of occurrence of ionospheric irregularity) less than 0.05 are 97.3, 89.4, and 81.3, respectively.

© 2015 Elsevier Ltd. All rights reserved.

1. Introduction

Several projects have been running in Africa since the last decade to analyse and test the future use of Space Based Augmentation System (SBAS), in particular, the European Geostationary Navigation Overlay Service (EGNOS). The examples of the projects include: the Euro-Mediterranean (EUROMED), Satellite navigation services for African Region (SAFIR), SBAS Awareness and Training for South Africa (SATSA), and Training on EGNOS – Global Navigation Satellite Systems (GNSS) in Africa (TREGA). The SBAS involves correcting for the positioning errors due to ionospheric propagation delay or phase advance, depending on the observable. In addition to positioning errors due to propagation delay or phase advance, the problem caused by the ionosphere in the African low latitude regions may include scintillations and loss of locks in severe cases due to small-scale ionospheric

irregularities (Lonchay et al., 2014). Scintillations and loss of locks result into cycle slips (CS), usually observed as sudden phase jumps. Apart from ionospheric irregularities, other sources of CS events are obstructions of the satellite signal, multi-path, and a failure in the receiver software (Hofmann-Wellenhof et al., 2007). Therefore, scintillations and loss of locks due to ionospheric irregularities degrade and disrupt satellite-based communications and navigation systems (Secan et al., 1995; Paznukhov et al., 2012).

Due to their adverse effects on trans-ionospheric signals, modelling the ionospheric irregularities has been undertaken by several researchers in the past. The first global empirical model for the quiet time *F* region equatorial vertical drifts based on combined incoherent scatter radar observations at Jicamarca and ion drift meter observations on board the Atmospheric Explorer E satellite was presented by Scherliess and Fejer (1999). By using a 5-year series of observations at 254 MHz taken at Huancayo, Peru, Aarons (1985) developed analytical equation to yield scintillation excursions as a function of solar flux, magnetic index, local time, and day of the year. Iyer et al. (2006) developed an empirical model of magnetic quiet time scintillation occurrence at Indian

* Corresponding author.

E-mail address: pmungufeni@gmail.com (P. Mungufeni).

equatorial and low latitudes. [Abdu et al. \(2003\)](#) developed a regional model for the quiet-time spread *F* distribution in the Brazilian longitude sector.

Much as there exists some efforts to model the ionospheric irregularities globally and in other equatorial regions of the world, there is no specific and suitable model for the African low latitude regions. This study therefore aimed to develop empirical models for the probability of occurrence of ionospheric irregularities (OII) during quiet geomagnetic conditions. GNSS-derived ionospheric total electron content (TEC) over Mbarara, Uganda (0.60°S, 30.74°E, geographic) and Libreville, Gabon (0.35°N, 9.68°E, geographic) has been separately used to develop models of probability of OII. These two stations in the African low latitude region have extensive GNSS data base. In [Sections 2](#) and [3](#), the data sources and the methods employed in this study are discussed, respectively. The results which mainly focused on the validation of the models are presented and discussed in [Section 4](#). The conclusions of the study are presented in [Section 5](#).

2. The data

The International GNSS Service (IGS) for Geodynamics stations at Libreville, Gabon (NKLK) and Mbarara, Uganda (MBAR) shown with triangles in [Fig. 1](#) have fairly adequate data for more than one complete sunspot cycle in the African low latitude region. Therefore, to capture the diurnal, seasonal, and sunspot cycle patterns of probability of OII for a complete sunspot cycle, this study used data from these two stations. Since the geometry of the arrangement of the stations does not favour inclusion of latitudinal dependence of OII in the model, we developed using the same technique a model over each station. The model developed over MBAR was validated with data over Mt. Baker, Uganda (BAKC) (0.35°N, 29.90°E, geographic), Kigali, Rwanda (NURK) (1.94°S, 30.09°E, geographic), and Kampala, Uganda (KAMP) (0.34°N, 32.60°E, geographic). The geographic distribution of the data sites used in this study for modelling and validation is shown with triangles in [Fig. 1](#). This figure also shows the geomagnetic equator with a black solid line and the anomaly crests geomagnetic latitudes ($\pm 15^\circ$) in Africa with dotted lines. The summary of information about the data sites used are presented in [Table 1](#).

The agencies that deployed GNSS receivers used in this study are: SCintillation Network and Decision Aid (SCINDA), University NAVstar Consortium (UNAVCO), and the IGS. The GPS-SCINDA system is a network of ground based receivers established by the Air Force Research Laboratory in collaboration with Boston College, both from the USA to provide regional specification and short term forecast of scintillations caused by electron density irregularities in the equatorial ionosphere ([Groves et al., 1997](#)). The UNAVCO is a non-profit University-governed consortium that facilitates geo-science research and education using geodesy ([Ware, 1995](#)). The IGS is a voluntary federation of worldwide agencies that are committed to providing the highest quality data and products as the standard for GNSS in support of Earth science research, multi-disciplinary applications, and education ([Melbourne and Neil, 1995](#)).

The Receiver INdependent EXchange (RINEX) data files (navigation and observation) were used. For the IGS stations, the RINEX files were obtained from Scripts Orbit and Permanent Array Center (SOPAC).¹ The GPS-SCINDA data from KAMP was provided by the Physics Department of Makerere University, while the data of BAKC was obtained from UNAVCO website. The RINEX files were processed using GPS-TEC analysis application software ([Seemala](#)

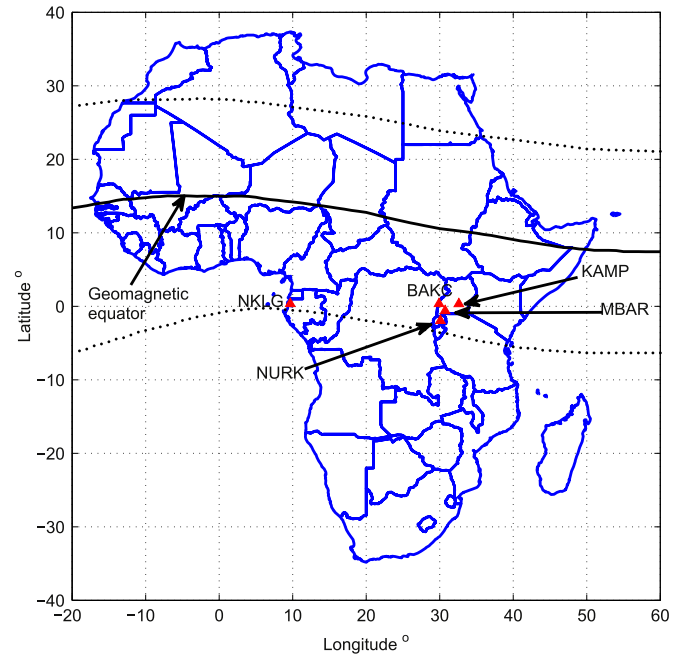


Fig. 1. African map showing: (i) locations of IGS stations, MBAR, NKLK, BAKC, NURK, and GPS-SCINDA, KAMP with triangles; (ii) the geomagnetic equator (black solid line); and (iii) anomaly crests geomagnetic latitudes $\pm 15^\circ$ (dotted lines).

Table 1
GNSS receivers used in the study.

Country	Location	Code	Organisation	Geog. lat. (°N)	Geog. lon. (°E)	Mag. lat. (°N)
Uganda	Kampala	KAMP	SCINDA	0.34	32.60	-9.29
Gabon	Libreville	NKLK	IGS	0.35	9.68	-8.05
Uganda	Mbarara	MBAR	IGS	-0.60	30.74	-10.22
Uganda	Mt. Baker	BAKC	UNAVCO	0.35	29.90	-9.25
Rwanda	Kigali	NURK	IGS	-1.94	30.09	-11.62

and [Valladares, 2011](#)) to obtain Vertical TEC (VTEC) values and elevation angles of the various satellites tracked as a function of UT. Usually, $1 \text{ TECU} = 10^{16}$ electrons per m^2 .

The VTEC data for quiet geomagnetic days ($K_p \leq 3$) were considered in order to isolate the OII due to storms ([Li et al., 2008](#)). Quiet geomagnetic days were identified by examining the 3 hourly K_p index obtained from the World Data Center of Kyoto, Japan.² The K_p index measures the overall level of geomagnetic disturbance. Daily solar Flux index, $F_{10.7}$, obtained from Space Weather Prediction Center (SWPC) of the National Oceanic and Space Administration (NOAA)³ were used to bin data of the respective days into different solar flux levels.

3. The method

Ionospheric irregularities of electron density can be studied using the rate of change of total electron content (ROT) which can be determined using the expression ([Aarons et al., 1996](#); [Pi et al., 1997](#))

$$\text{ROT} = \frac{\text{VTEC}_k^i - \text{VTEC}_{k-1}^i}{t_k^i - t_{k-1}^i}, \quad (1)$$

² <http://swdcwww.kugi.kyoto-u.ac.jp/>

³ <http://www.swpc.noaa.gov/>

¹ <http://www.sopac.ucsd.edu>

where $VTEC_k^i$ and $VTEC_{k-1}^i$ are consecutive VTEC values at epochs t_k^i and t_{k-1}^i corresponding to observed satellite i . The ROT can provide information on the spatial variation of electron density (Basu et al., 1999). At low and mid-latitudes, for high elevation angles, the fluctuations in ROT are due to ionospheric irregularities with scale-sizes of several hundred meters to about 2.5 km (Pi et al., 1997). This value also depends on plasma drift velocities. To identify and statistically present the smaller scale irregularities, Pi et al. (1997) defined the rate of change of TEC index (ROTI) by taking the standard deviation of ROT over a 5-min period. According to Zou and Wang (2009), large and small-scale ionospheric irregularities at scale-lengths of a few kilometers and ~400 m can be investigated simultaneously with the ROT and ROTI indices.

In this study, before computing the ROTI, VTEC measurements with satellite elevation angle greater than 30° were considered in order to minimise the effects of multi-path on the observations. The ROTI computations were further limited to measurements made from satellites that were locked on for greater than 4 min to allow the receivers de-trending filter to stabilise, in case it had lost lock on the carrier phase. The ROTI values for all the satellites in view at the end of every 5 min (basic interval for computing the ROTI) were averaged to obtain 5 min resolution data for a day.

3.1. Cycle slips and ionospheric irregularities

The median value of ROTI, M_{ROTI} , at epochs of observing CS associated with ionospheric irregularities was considered as a threshold for OII. The carrier-phase measured in whole cycles at L-band frequencies L1 (1.57542 GHz) and L2 (1.2276 GHz), Φ_1 and Φ_2 , respectively, available in RINEX observation files was used to determine the occurrence of CS. Examples of methods of CS detection include, phase and code range combinations, doppler integration, differentials of phases with respect to time, and phase combinations (Guochang, 2007; Hofmann-Wellenhof et al., 2007). In this study, we used phase combinations. A parameter P identical to ionospheric residual was computed using the equation (Hofmann-Wellenhof et al., 2007):

$$P = \Phi_1 - \frac{L1}{L2}\Phi_2. \tag{2}$$

If there are no CS, the temporal variations of P would be small, for normal ionospheric conditions and for short baselines. Indicators of CS events are sudden jumps in successive values of P . The parameter P contains only frequency dependent parameters (see Eq. (2)), depends on the ionosphere (and multipath), and varies slowly with time. This geometry-free method is good for a single receiver and does not need a priori knowledge of station or satellite coordinates (Gunter, 2003).

To demonstrate CS and its detection using parameter P , we present in Fig. 2 the variation of phase on L1 (left column panels) and P (right hand-side panels) for some satellites on March 23, 2002 at MBAR. The satellites are identified with pseudo-random numbers (PRN). The PRN's 26 and 27 indicate loss of lock (LL), while satellites with PRN 1, 7, 10 experienced CS, marked CS in Fig. 2. It can be seen in the right hand side panels of Fig. 2 that at the epoch of CS or LL, there is a sudden jump in P value. Particularly, we identified CS when a difference of greater than 2 occurred in the successive values of P . The sudden jump in P value for PRN 26 might not be clearly visible due to the large units of both the phase and P indicated in Fig. 2.

Several studies have shown that ionospheric irregularities occur mainly after sunset (Wanninger, 1995; Amabayo et al., 2011; Olwendo et al., 2013), in the equinox months (Paznukhov et al., 2012; Amabayo et al., 2011; Olwendo et al., 2013; D'ujanga et al., 2013), and in high solar activity years (Aarons, 1993; Basu et al., 1988). Bearing these points in mind, to increase chances of the observed CS events being due to ionospheric irregularities, but not other causes as stated in Section 1, we searched for CS events from 19:30 LT to 03:00 LT in equinox months (March, April, September, and October) in the years, 2001–2004. In the search, when tracking a particular satellite, in epochs of every 5 min (interval over which the ROTI is defined), occurrence or non-occurrence of CS event and ROTI value was determined. The values of ROTI at the epochs with CS were noted. For all the satellites tracked in the entire stated period of searching CS events, the median of ROTI values at the epochs of observing CS events was determined to represent background ionospheric irregularity level.

The number of geomagnetically quiet nights in which CS were searched over MBAR and NKLK was 87 and 151, respectively. Table 2 presents the information on the number of nights per year

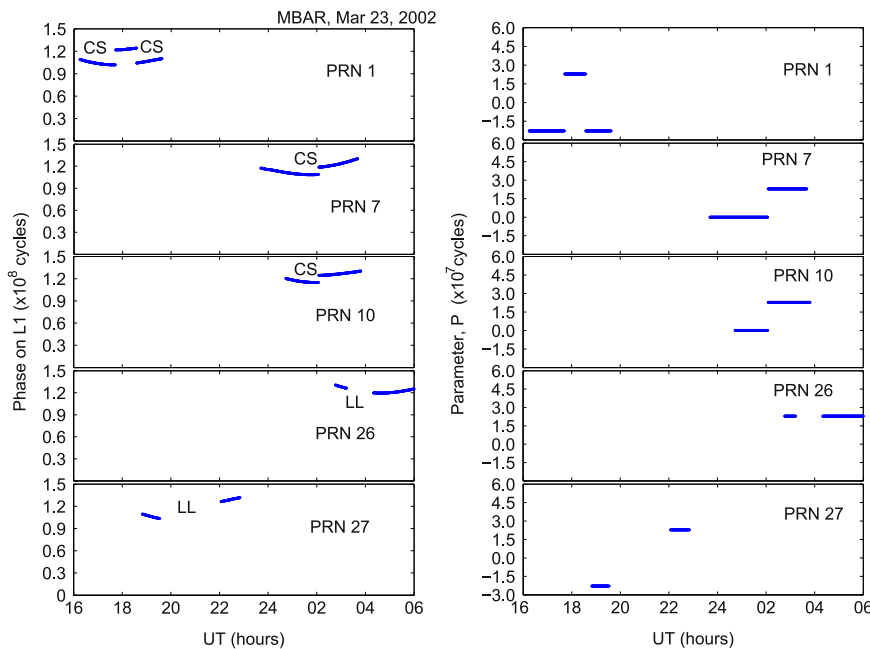


Fig. 2. Variation of phase on L1 (Left column panels) and P (right hand side column panels) for some satellites on March 23, 2002 at MBAR.

Table 2

Number of nights, CS events, and median of ROTI at epochs of observing CS at MBAR and NKLK during 2001–2004.

Year	MBAR			NKLK		
	Nights	CS events	ROTI (TECU/min)	Nights	CS events	ROTI (TECU/min)
2001	25	136	0.60	44	53	0.44
2002	29	168	0.81	45	48	0.47
2003	–	–	–	06	05	0.05
2004	33	56	0.16	82	92	0.55

over each station CS were observed. The number of CS per year and the corresponding median ROTI value at the epochs of observing CS is also presented in the table. Overall, over the two stations, a total of 699 CS associated with ionospheric irregularities were observed. The median ROTI value at the epochs of observing the 699 CS was 0.54 TECU/min. Basing on these analyses, any ROTI value ≤ 0.5 TECU/min was considered as background ionospheric irregularity level. Note that Tanna et al. (2013) and Ma and Maruyama (2006) considered ROTI < 0.5 TECU/min as background ionospheric irregularity level in India and Japan, respectively.

3.2. Treatment of data

The data for the quiet day ionospheric irregularity levels (ROTI), for the stations NKLK and MBAR during 2001–2012 were grouped into 3 bins. The bins had $F_{10.7}$ value ranges that represented low

solar activity (LSA), medium solar activity (MSA), and high solar activity (HSA) levels. We considered in sunspot cycle 23 the years 2003 and 2005 as the end of high solar activity and medium solar activity periods, respectively. The lower limit (120) of the high solar activity level bin corresponded to the median of $F_{10.7}$ of the year 2003. The lower limit of medium solar activity level bin (80) corresponded closely to the median of $F_{10.7}$ of the year 2005. Therefore, the three bins had $F_{10.7}$ value ranges as $F_{10.7} < 80$, $80 \leq F_{10.7} \leq 120$, and $F_{10.7} > 120$ for LSA, MSA, and HSA levels, respectively. The data in each of the bins were grouped into 12 months of the year which were further arranged in LT bins. Since ionospheric irregularities tend to occur after sunset and in some cases they can be observed even after midnight, the LT bins ranged from 18:00 to 06:00. During 18:00–20:00 LT and 03:00–06:00 LT, the LT bins had resolution of 1 h. However, during 20:00 LT–03:00 LT, when the peak of OII is expected, 30 min resolution was applied. The probability of OII, P_{irr} at each LT of a given month and a given solar flux range bin were calculated using the equation:

$$P_{irr} = \frac{\text{Number of ROTI} > M_{ROTI}}{\text{Total number of observed ROTI}} \tag{3}$$

Fig. 3 presents the available number of ROTI values, used to compute P_{irr} which in turn were used in the model that was developed over MBAR (left column panels) and NKLK (right column panels). From this point onwards, the number of ROTI is referred to as the number of samples. The top, middle, and bottom panels present the number of samples used as a function of LT and month during LSA, MSA, and HSA, respectively. For a month whose number of samples in a typical 1 h interval, derived from 7 days

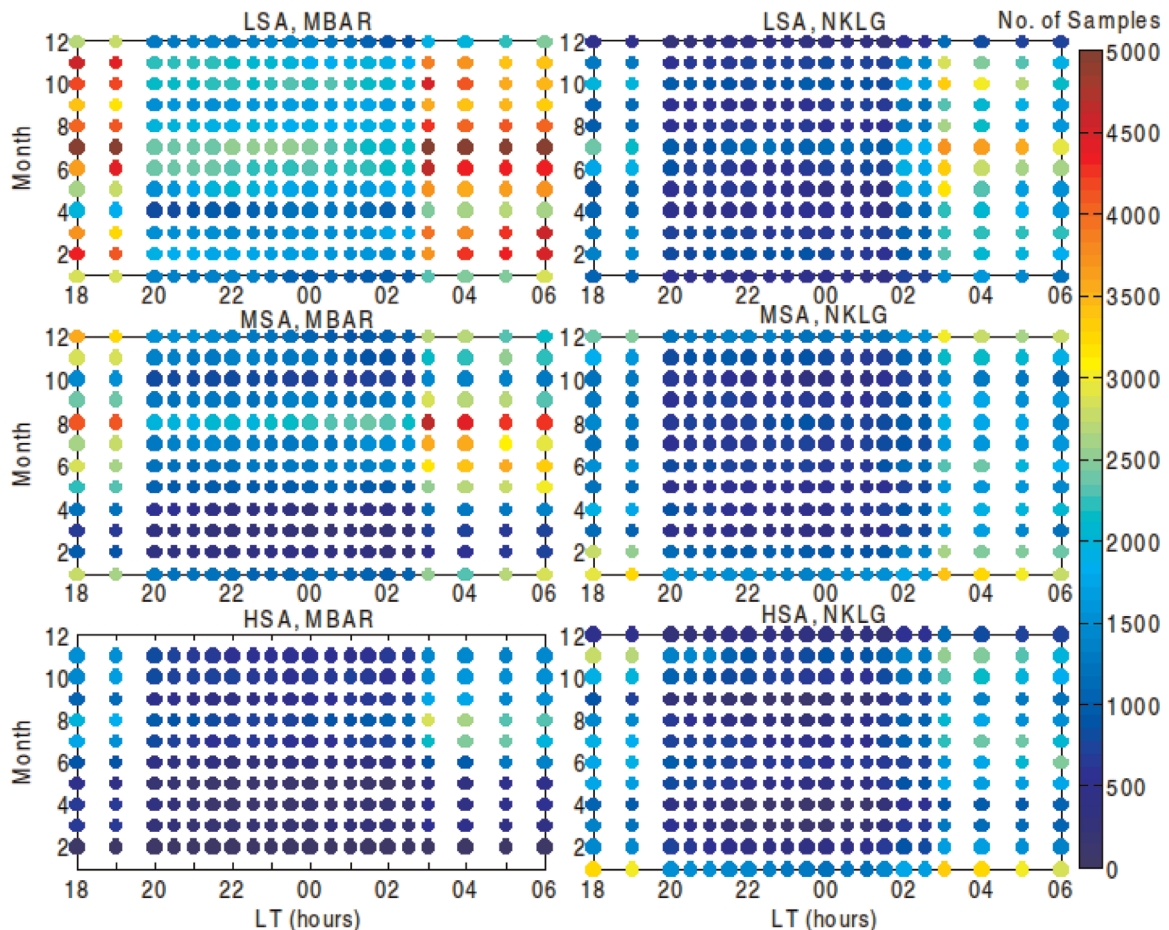


Fig. 3. Number of available samples as a function of month and LT over MBAR (left column panels) and NKLK (right column panel). Top, middle, and the bottom panels are for LSA, MSA, and HSA months, respectively. The colour bar ranges from blue (low number of samples) to red (high number of samples).

data would be 336 (number of ROTI values in 1 h (12) multiplied by 7 multiplied by the nominal number of satellites that can be viewed above 30° elevation at any time (4)). Therefore, we refer to number of samples ≥ 300 being adequate, providing good representation. At MBAR, it can be noted from left hand column panels in Fig. 3, the months of LSA are well represented at all epochs. Most months of MSA are also well represented, except February–April. For HSA, the months that have not been well represented (number of samples < 300) at some or all epochs range from February to June. Unfortunately, January and December of HSA are not represented at all.

At NKLK (right hand column panels in Fig. 3), the top panel shows that the LSA months of April, May, August, and December are not well represented at some epochs. The middle panel indicates that all the months of MSA have been well represented. The bottom panel shows that the HSA months of February–April and August–September have not been well represented at some epochs.

3.3. The model

A spline function of order n , with knot sequence \vec{t} is any linear combination of Basis-splines (B-splines) of order n for the knot sequence \vec{t} (De Boor, 2001). A group of spline functions forms the spline space. Generally, the probability of OII as a function of LT (t), month (m), and solar flux (F) can be expressed as a spline space using the equation (Abdu et al., 2003; Iyer et al., 2006)

$$P(t, m, F) = \sum_{i=1}^{20} \sum_{j=1}^{12} \sum_{k=1}^3 a_{i,j,k} N_{i,4}(t) N_{j,2}(m) N_{k,2}(F), \quad (4)$$

where $N_{i,4}(t)$ is a cubic B-spline of order four applied to LT dependence (t). $N_{j,2}(m)$ and $N_{k,2}(F)$ are cubic B-splines of order two applied to monthly or seasonal (m) and solar flux (F) dependences, respectively. Because of the rapid changes in P_{irr} with LT, especially after sunset, a higher order ($N_{i,4}(t)$) cubic B-spline was used to represent LT dependence (Scherliess and Fejer, 1999). The coefficients $a_{i,j,k}$ were determined by a least squares fit to the binned data. The various nodes were determined in a similar way as in Scherliess and Fejer (1999), Abdu et al. (2003), and Iyer et al. (2006). Twenty local time nodes were used and distributed between 18:00 and 06:00 LT. For simple interpolation between months, seasonal/monthly nodes were placed at the 15th day of each month. Solar flux nodes each representing weighted value within the respective solar flux range bin for each month, that were determined and used to develop models over MBAR and NKLK, are shown in Table 3.

4. Results and discussion

By considering $M_{ROTI} = 0.5$ in Eq. (3), the probabilities of OII as a function of LT, month, and solar flux have been computed and modelled using Eq. (4).

4.1. Comparison of model with observations

Fig. 4 presents the comparison of the probability of OII obtained from the binned data as a function of month and LT (left panels) with the modelled data (right panels) over MBAR. The top, middle, and bottom panels correspond to LSA, MSA, and HSA levels, respectively. The colour bar ranges from blue (low probabilities) to red (high probabilities). The white space in the bottom panels shows missing data. At all solar flux levels, and particularly during equinox months, the binned data shows that the starting time of

Table 3
Solar flux nodes used in the model.

Month	$F_{10.7}$ flux (MBAR)			$F_{10.7}$ flux (NKLK)		
	High	Moderate	Low	High	Moderate	Low
January		86	73	176	87	76
February	122	90	74	168	98	75
March	179	89	73	166	96	74
April	187	97	71	182	97	73
May	176	93	72	160	95	72
June	144	97	71	155	96	70
July	150	91	70	147	91	71
August	154	95	69	158	94	70
September	170	96	70	182	90	69
October	167	95	72	160	87	71
November	170	96	73	173	92	72
December		94	72	181	90	71

observing probability of OII values greater than 0.1 is just after 20:00 LT, lasting up to about 01:00 LT. Moreover, the observed binned data shows that the peak of probability of OII mostly occurs at about 22:30 LT. As seen in the right hand-side panels of Fig. 4, these diurnal patterns in probability of OII have been reproduced by the model.

Theoretically, plasma bubbles are formed after sunset as a result of much faster recombination at lower altitudes than at higher altitudes. Therefore, a steep upward plasma density gradient exists between the bottom side ionosphere and the upper F region (Li et al., 2008). This produces the classical configuration for the Rayleigh–Taylor (R–T) instability (Schunk and Nagy, 2009; Kamide and Maltsev, 2007). In the generalised R–T instability, during the day, the zonal electric field in the lower ionosphere is eastward due to the thermospheric winds orientation in the same direction (Kelley, 2009). The eastward electric field, in combination with the northward B field, produces an upward $E \times B$ drift of the F region plasma. The general condition for instability is that the $E \times B$ direction be parallel to the plasma density gradient.

Apart from the effect of the eastward electric fields on the F region plasma during the day, the evening equatorial F region often shows enhanced vertical drifts, also known as the Pre-Reversal vertical drift velocity Enhancements (PRE). Under PRE, the depleted plasma of the lower heights rise up to the topside ionosphere in the form of plasma bubbles or irregularities (Fejer and Scherliess, 1999; Li et al., 2008; Basu et al., 1999; Cervera and Thomas, 2006). In addition to vertical drifts of up to heights of 1000 km, the irregularities map poleward along the magnetic field lines until they reach the Appleton anomaly regions ($\pm 15^\circ$ geomagnetic latitude) (Zou and Wang, 2009).

In line with the described theory, Wanninger (1995) stated that scintillation occurs approximately between 1 h after sunset and midnight, and occasionally continues until dawn. Therefore, our observations of increased P_{irr} mostly during 20:00–00:00 LT is within this frame.

The model has also captured the solar activity dependence very well. In Fig. 4 the observed data shows that as the solar activity increases (top to bottom in the panels), the probability of OII also increases, especially during equinox months. This solar activity dependence of OII has been captured by the model as shown in the right hand panels of Fig. 4.

The low observations of P_{irr} during low and moderate solar activity conditions could be due to low electron density in the post-sunset period in this condition (Aarons, 1993). Basu et al. (1988) used extensive VHF/UHF scintillation data base at the equatorial (American sector), equatorial anomaly (Pacific sector), and a high latitude region to determine the magnitudes of phase and intensity scintillations and their temporal structures during

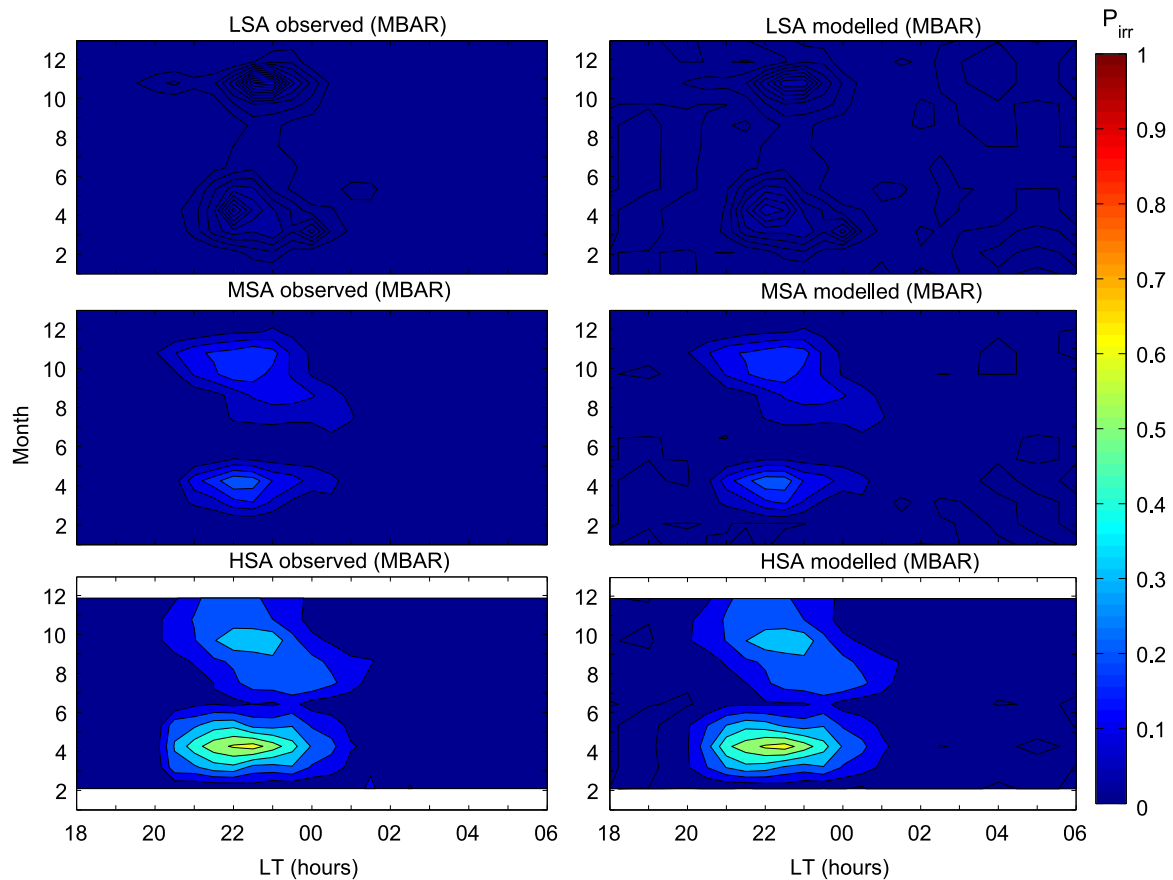


Fig. 4. Panels on the left present contour plots of computed probability of OII over MBAR, while panels on the right present contour plots of modelled probability of OII. Top, middle, and bottom panels correspond to LSA, MSA, and HSA levels, respectively. The colour bar ranges from blue (low P_{irr}) to red (high P_{irr}).

the sunspot maximum and minimum periods. They found a strong solar activity control of scintillation activity at all regions. [Aarons \(1993\)](#) stated that years of high solar flux bring about both higher occurrence of equatorial irregularities and higher scintillation intensities.

Another aspect captured by the model is the seasonal dependence of the probability of OII. Particularly in MSA and HSA, the increased probabilities of OII in Mar equinox and Sep equinox in the observed data have been reproduced by the model.

The seasonal dependence of P_{irr} observed is consistent with those reported by [Wanninger \(1995\)](#), [Paznukhov et al. \(2012\)](#), [Olwendo et al. \(2013\)](#), and [D'ujanga et al. \(2013\)](#). The production of the ionosphere is dependent mainly on the intensity of the ionising radiation from the Sun. The intensity of the ionising radiation varies with the elevation of the Sun ([Hargreaves, 1992](#)). In equinox months, the elevation of the Sun is high at the low latitudes in the African region. This means increased ionisation and the occurrence of severe ionospheric irregularities.

[Fig. 5](#) is similar to [Fig. 4](#), but for NKLG. The figure has also demonstrated that the model is capable of capturing the diurnal, seasonal, and solar flux dependence patterns of probability of OII. The outstanding difference between [Figs. 5](#) and [4](#) is: both the observed data and the modelled data of [Fig. 5](#) show that there is a secondary peak in probability of OII at about 01:00 LT, especially during Mar equinox.

[Valladares et al. \(2004\)](#) stated that the polarisation electric fields vary greatly in LT and latitude. Since NKLG and MBAR have different local times and latitudes, it is possible to experience a secondary peak in P_{irr} over NKLG (see [Fig. 5](#)), and not over MBAR. The observation of a secondary peak in P_{irr} in both the observed

and modelled data over NKLG may be due to the closeness of NKLG to the dip equator. The poleward mapping of the ionospheric irregularities might have diminished considerably at dip latitude of MBAR ($\sim 10.22^\circ$ S), while at the dip latitude of NKLG ($\sim 8.05^\circ$ S) the mapping might still be significant. Generally, it has been observed that ionospheric irregularities over the western low latitudes in Africa are stronger than those in the east ([Paznukhov et al., 2012](#)). More work needs to be done to understand exactly the mechanism for the occurrence of a secondary peak in the probability of OII over NKLG.

In addition to validating the models using the binned data ([Figs. 4](#) and [5](#)), we computed the P_{irr} in the months of the years 2002, 2005, and 2008. These years represent HSA, MSA, and LSA periods, respectively. [Fig. 6](#) presents the comparison of the computed P_{irr} with the corresponding modelled P_{irr} over MBAR (panels (a)–(c)) and NKLG (panels (d)–(f)). The blue line and the green markers represent the observed data and the modelled data, respectively. It is important to remember that the LT for the comparison in a month ranges from 18:00 to 06:00. For clarity purposes, the LT marks were not labelled in [Figs. 6](#)–[9](#). In [Fig. 6](#), the observed data (blue solid curve) shows that the probability of OII begins to increase at about 20:00 LT, peaking at about 23:00 LT. By about 01:30 LT the probability of OII vanishes. These diurnal patterns are closely approximated by the model (green markers) and are clearly exhibited in equinox months, in the years 2002 and 2005. In the year 2008, mostly probability of OII values close to zero are observed both in the measured and modelled data. The close approximation by the model of the patterns exhibited by the observed data during 2002, 2005, and 2008 in the different seasons suggests that the models developed over each of the station

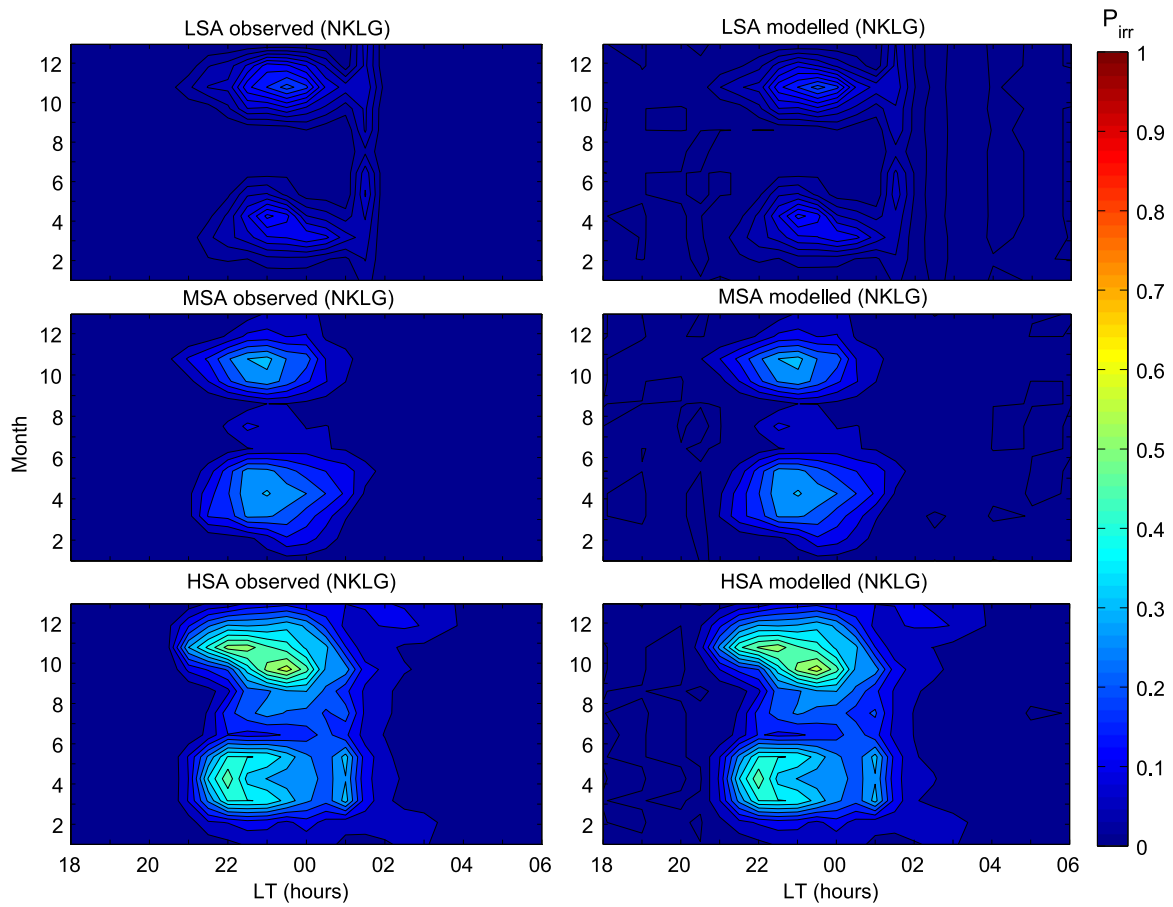


Fig. 5. Similar to Fig. 4, but for NKL.

is capable of capturing diurnal, seasonal, and solar activity dependence patterns of probability of OII over the respective station.

However, cases of discrepancies between the observed and the modelled probability of OII can be visualised in Fig. 6. Over MBAR

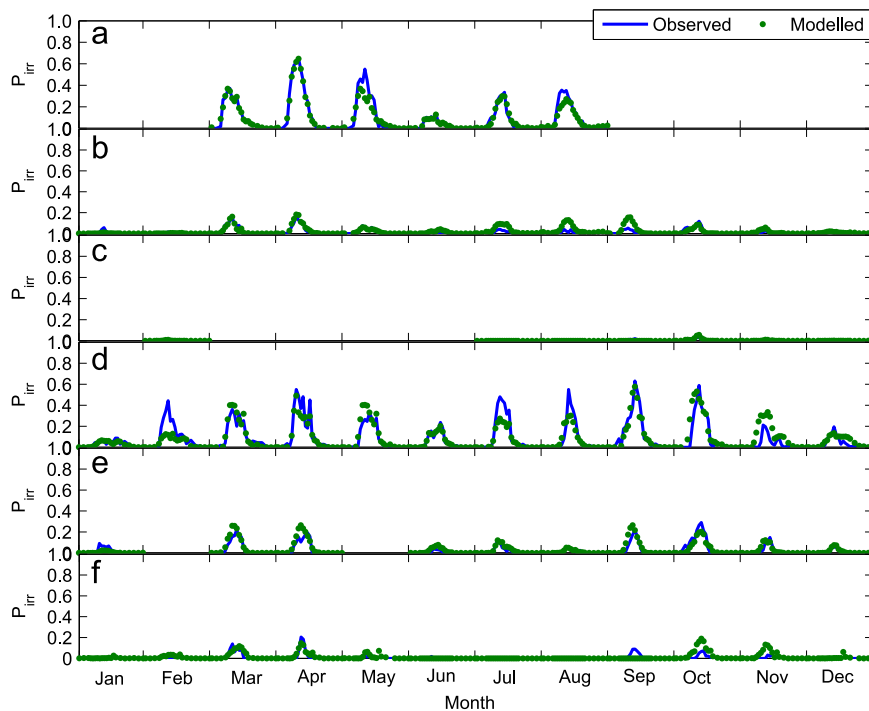


Fig. 6. Comparison of measured probability of OII with modelled values over MBAR (panels (a)–(c)) and NKL (panels (d)–(f)) for the years 2002, 2005, and 2008. Blue and green dotted lines represent observed and modelled values, respectively. (For interpretation of the references to colour in this figure caption, the reader is referred to the web version of this paper.)

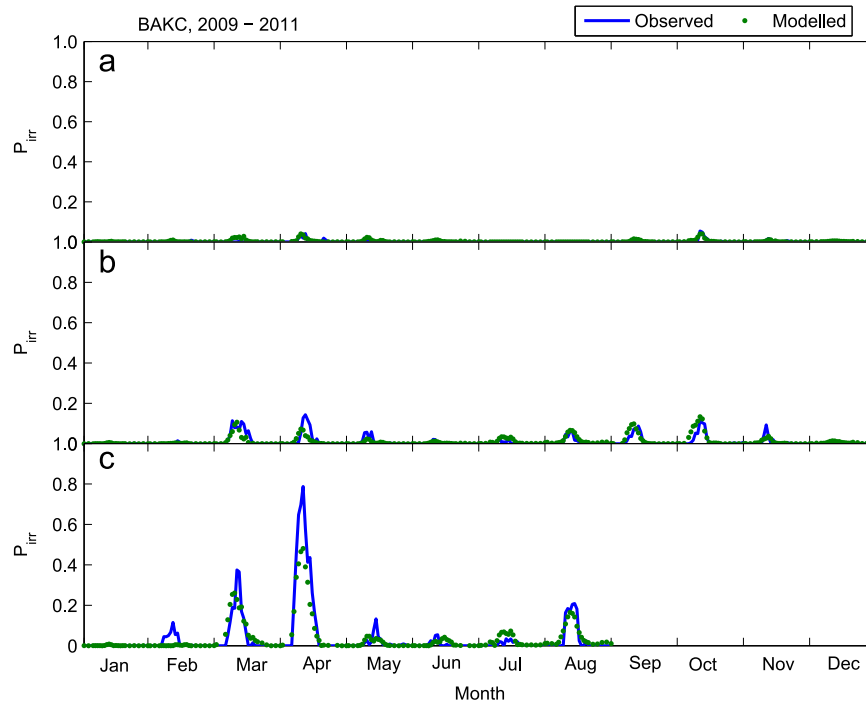


Fig. 7. Comparison of measured probability of OII with modelled values over BAKC. Panels (a), (b), and (c) are for the years 2009, 2010, and 2011, respectively. Blue and green dotted lines represent observed and modelled values, respectively. (For interpretation of the references to colour in this figure caption, the reader is referred to the web version of this paper.)

discrepancies exist in May and September, 2005, while over NKLK, discrepancies exist in February, July, and August, 2002, and September, 2008. Mostly, these discrepancies are due to inadequate data used in the computation of probability of OII over each station in the affected months.

Next, we validated the model developed over MBAR with data over stations away from MBAR. Due to unavailability of a station with data in the same LT zone as NKLK, we did not validate further the model over MBAR,

data from BAKC, KAMP, and NURK were used. These stations are close to MBAR (see Fig. 1) and they are also approximately in the same LT zone.

Fig. 7 presents the comparison of observed probability of OII with the modelled values over BAKC. Panels (a), (b), and (c) are for the months of the years 2009, 2010, and 2011, respectively. In Fig. 7, the observed data (blue solid curve) and the modelled data (green markers) exhibit diurnal, seasonal, and solar activity dependence patterns similar to those discussed over MBAR and

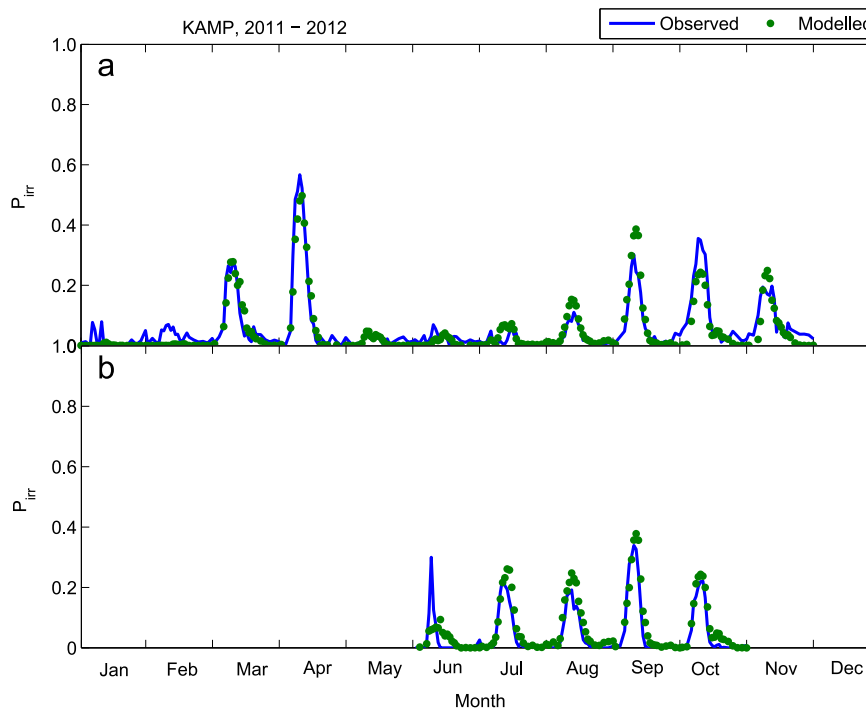


Fig. 8. Similar to Fig. 7, but for KAMP.

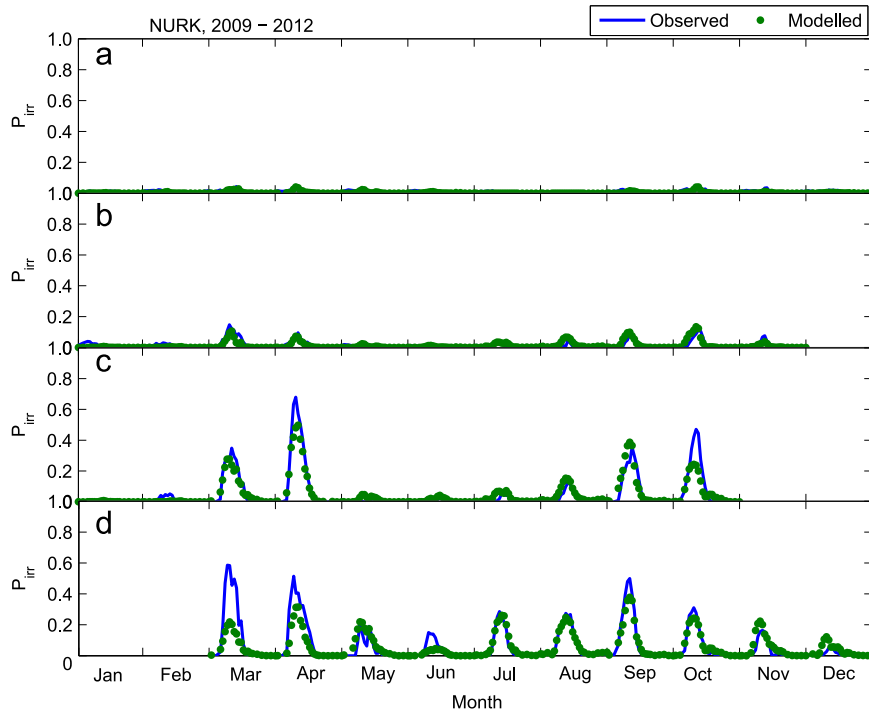


Fig. 9. Similar to Figs. 7 and 8, but for NURK.

NKLG (Fig. 6). The close approximation by the model of the patterns exhibited by the observed data during 2009–2011 in the different seasons suggests that the model is capable of capturing diurnal, seasonal, and solar activity dependence patterns of probability of OII over BAKC. Note that the yearly mean $F_{0.7}$ flux during 2009–2011 ranges from about 71 to 113. In most cases, Fig. 7 has shown that the model over MBAR station approximates

closely the probability of OII over BAKC at a distance of about 137.64 km (north west). The discrepancies between the modelled and the measured data in Figs. 7–9 have been quantified with the monthly root mean squared errors (rmse) in the months validated. These discrepancies and the rmse will be discussed later.

Fig. 8 is similar to Fig. 7, but for KAMP. Panels (a) and (b) are for the months of the years 2011 and 2012, respectively. The diurnal

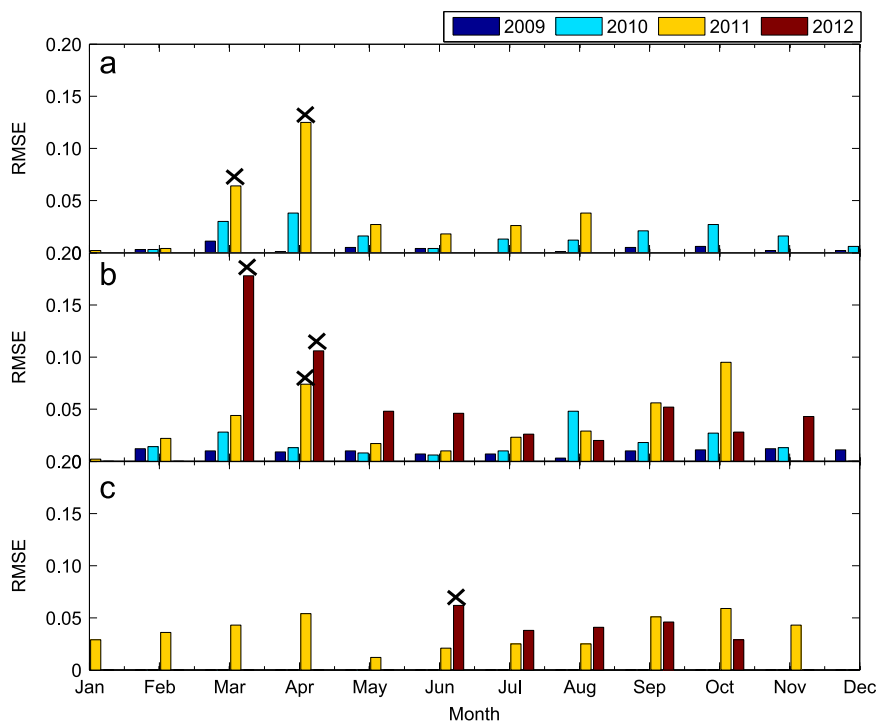


Fig. 10. Monthly root mean squared errors in the comparison of the modelled and the observed P_{irr} during (a) 2009–2011 over BAKC, (b) 2009–2012 over NURK, and (c) 2011–2012 over KAMP. The crosses indicate months where the number of samples used in either the model or month to be validated was inadequate. Blue, cyan, yellow, and red bars represent the rmse values during 2009, 2010, 2011, and 2012, respectively.

and seasonal patterns of observed and the modelled P_{irr} shown in Fig. 8 are similar to those of BAKC (Fig. 7) that was discussed previously. Generally, Fig. 8 has shown that the model over MBAR also tries to approximate closely the diurnal and seasonal dependence of probability of OII over KAMP, at approximate straight line distance of about 237.61 km (north-east).

Fig. 9 is similar to Figs. 7 and 8, but for NURK. Panels (a), (b), (c), and (d) are for the months of the years 2009, 2010, 2011, and 2012, respectively. The increasing trend of both observed and modelled probability of OII during 2009–2012 (increasing solar activity, with mean yearly $F_{10.7}$ flux ranging from 71 to 120) can be visualised in Fig. 9, particularly in equinox months. The diurnal patterns of both observed and the modelled probability of OII are similar to those discussed for the validation over BAKC. In summary, apart from the few cases of the inability of the model developed over MBAR to accurately predict the probability of OII, most of the months have exhibited fairly good comparison between the observed and the modelled probability of OII. The model developed over MBAR captured the diurnal, seasonal, and solar activity dependence patterns of probability of OII over NURK (straight line distance of approximately 162.42 km, south-west of MBAR).

Most discrepancies between modelled and observed data in Figs. 7–9 depict that the model underestimates the P_{irr} over BAKC and NURK, while it overestimates the P_{irr} over KAMP. Fig. 10 presents the monthly rmse for the comparison of the modelled and the observed P_{irr} during (a) 2009–2011 over BAKC, (b) 2011–2012 over KAMP, and (c) 2009–2012 over NURK. In the figure, the bars for rmse in the months with inadequate data used to either develop the model over MBAR or validate it are marked with crosses. Blue, cyan, yellow, and red bars represent the rmse values during 2009, 2010, 2011, and 2012, respectively.

In order to link the performance of the model during validation in the various months to the available number of samples used in development of the model (Fig. 3), it is important to note the solar flux levels of the months validated at each station. For this reason, the average of the daily solar flux values of the days considered in each of the months validated in Figs. 7–9 were computed. For BAKC, the averages for the months of the year 2009 show that they belong to LSA conditions. Apart from the months, April–June of the year 2010 that have been categorised as LSA months, the rest have been identified as MSA months. In the year 2011, all the months fall in the group of MSA. For KAMP, the months of October and November, 2011 belong to HSA conditions. The rest of the months considered in 2011 and 2012 have been identified as MSA months. While for NURK, apart from the months January–March and July–November of the year 2010, the rest of the months considered in the years 2009 and 2010 have been identified as LSA months. With the exception of September and October that have been identified as HSA months, the rest of the months in the years 2011 and 2012 have been categorised as MSA months.

The underestimation of the P_{irr} by the model at BAKC (Fig. 7, panel (c)) in March and April, 2011 has been reflected in the large rmse observed in Fig. 10, panel (a), in the respective months. These disagreements could be due to the low number of samples available in these months of MSA as shown in Fig. 3.

For the validation at KAMP (Fig. 8, panel (b)), the visible difference between the observed and the modelled data in June, 2012 has been manifested in the large rmse observed in that month. Since Fig. 3 has shown that the number of samples used in the model in June of MSA has been adequate, the discrepancies in this month might be due to the low number of samples from KAMP that was used in computing probability of OII in this month (not shown here).

The rmse values indicated in Fig. 10 (panel (b)) at NURK reveal poor prediction of the probability of OII by the model in April and October in 2011, and March–April, 2012. These high rmse values

quantified the discrepancies in the respective months and years in the corresponding Fig. 9. These discrepancies might be due to the low number of samples used in the model. For instance, the left bottom panel in Fig. 3 shows that in HSA, there has been a low number of available samples in March and April. The left middle panel in Fig. 3 shows that in MSA, there has been a low number of available samples in April, and fairly adequate available number of samples in October. The number of samples in October, 2011 at NURK for computing the probabilities of OII was adequate (not shown here). Basing on these analyses, the underestimation of the probability of OII by the model in October, 2011 over NURK may have a different cause. More investigations are needed to understand such circumstances.

The distribution of the model errors (difference between the observed probability of OII and the modelled probability of OII) at NURK, BAKC, and KAMP are presented in Fig. 11, panels (a), (b), and (c), respectively. The errors presented at each station cover the entire period for which there were data available at each station. At the right end of each panel in Fig. 11, the total number of errors, mean error, the standard deviation, and the median are presented. It can be observed at all the three stations, the errors are random in nature (mean error is ≈ 0). The median and the standard deviation of the errors increase with increase in distance from MBAR. The percentages of the number of errors less than 0.05 at Mt. Baker, Kigali, and Kampala are 96.2, 92.7, and 83.3, respectively.

5. Conclusions

We have developed models of geomagnetically quiet time probability of occurrence of ionospheric irregularities over African low latitude region. GNSS-derived total electron content of the ionosphere data from Mbarara, Uganda and Libreville, Gabon during the period 2001–2012 were used. First, we established the ROTI value associated with background ionospheric irregularity over the region. This was done by analysing GNSS carrier-phases at L-band frequencies $L1 = 1.57542$ GHz and $L2 = 1.2276$ GHz with the aim of identifying cycle slip events. We identified over both stations, a total of 699 events of cycle slips. To increase the chances of cycle slips due to ionospheric irregularities, the search period was restricted to 19:30–03:00 LT in equinox months of the years, 2001–2004. The median ROTI value at the epochs of observing the 699 CS events was 0.54 TECU/min. Probability of occurrence of ionospheric irregularities associated with $ROTI \geq 0.5$ TECU/min was then modelled by fitting cubic B-splines to the data. The model developed over Mbarara was validated with data over Mt. Baker, Uganda (approximately, 137.64 km, north west), Kigali, Rwanda, (approximately, 162.42 km, south west) and Kampala, Uganda (approximately, 237.61 km, north east). For the period validated at Mt. Baker, Kigali, and Kampala the percentages of the number of errors (difference between the observed and the modelled probability of occurrence of ionospheric irregularity) less than 0.05 are 97.3, 89.4, and 81.3, respectively. The model performed well at the epochs when the number of samples used in the model was adequate. Apart from inadequate number of samples used in the model development, another limitation of the model could be low value of the upper limit of solar flux nodes (186 for MBAR and 182 for NKLK). The majority of the discrepancies in the months validated at BAKC and NURK show that the model underestimates the probability of OII, while the majority of the discrepancies in the months validated at KAMP show that the model overestimates the probability of OII. These may be due to the fact that the strength of ionospheric irregularities tends to reduce from west to east in the low latitudes in Africa (Paznu-khov et al., 2012). When more data becomes available over the region, these models will be combined to include a spatial

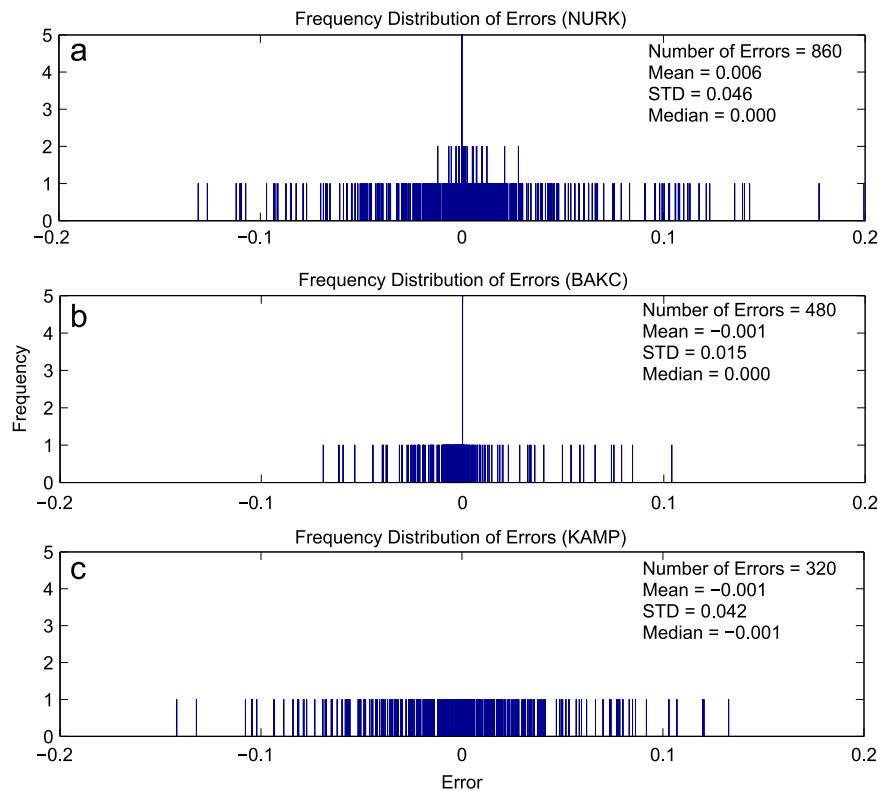


Fig. 11. Frequency distribution of the difference between the computed probability of OII and the modelled probability of OII at (a) NURK during 2009–2012, (b) BAKC during 2009–2011, and (c) KAMP during 2011–2012. Number of errors, mean error, standard deviation, and the median error are shown on the right extreme end of each panel.

dimension (longitudinal and latitudinal). In future, parameters that drive the occurrence of ionospheric irregularities during geomagnetically disturbed days will be established and incorporated in the model.

Acknowledgements

The International Science Program of Sweden financially sponsored this research (Code: UGA02). Part of the work was done at the T/ICT4D laboratory of the Abdus Salam International Center for Theoretical Physics based in Trieste, Italy when the first author visited the center during March–May, 2013 and January–March, 2014 as Junior Associate of the center. Thanks to the head of the T/ICT4D laboratory, Prof. Sandro Radicella and scientists Luigi Ciruolo, Bruno Nava, and Yenca Oru Migoya for their contributions and discussions during the research that led to results presented in this paper. J.B. Habarulema's contribution has been partly supported by the South Africa's National Research Foundation (NRF) Grant 90331. The data used in this study was obtained from <http://www.sopac.ucsd.edu>, <http://swdcwww.kugi.kyoto-u.ac.jp/>, and <http://www.swpc.noaa.gov/>.

References

- Aarons, J., 1985. Construction of a model of equatorial scintillation intensity. *Radio Sci.* 20 (3), 397–402.
- Aarons, J., 1993. The longitudinal morphology of equatorial F-layer irregularities relevant to their occurrence. *Space Sci. Rev.* 63, 209–243.
- Aarons, J., Mendillo, M., Yantosca, R., 1996. GPS phase fluctuations in the equatorial region during the MISETA 1994 campaign. *J. Geophys. Res.* 101 (12A), 26,851–26,862.
- Abdu, M.A., Souza, J.R., Batista, I.S., Sobral, J.H.A., 2003. Equatorial spread F statistics and empirical representation for IRI: a regional model for the Brazilian longitude sector. *Adv. Space Res.* 31 (3), 703–716.
- Amabayo, E.B., McKinnell, L., Cilliers, P.J., 2011. Statistical characterisation of spread F over South Africa. *Adv. Space Res.* (48), 2043–2052.
- Basu, S., Groves, K.M., Quinn, J.M., Doherty, P., 1999. A comparison of TEC fluctuations and scintillations at Ascension Island. *J. Atmos. Sol.-Terr. Phys.* 62, 1219–1226.
- Basu, S., MacKenzie, E., Basu, S., 1988. Ionospheric constraints on VHF/UHF communications links during solar maximum and minimum periods. *Radio Sci.* 23 (3), 363–378.
- Cervera, M.A., Thomas, R.M., 2006. Latitudinal and temporal variation of equatorial ionospheric irregularities determined from GPS scintillation observations. *Ann. Geophys.* 24, 3329–3341.
- De Boor, C., 2001. A practical guide to splines In: Marsden, J.E., Sirovich, L. (Eds.), *Applied Mathematical Sciences*, vol. 27. Springer, New York, USA.
- D'ujanga, F.M., Baki, P., Olwendo, J.O., Twinamsiko, B.F., 2013. Total electron content of the ionosphere at two stations in East Africa during the 24–25 October 2011 geomagnetic storm. *Adv. Space Res.* 51, 712–721.
- Fejer, B.G., Scherliess, L., 1999. Effects of the vertical plasma drift velocity on the generation and evolution of equatorial spread F. *J. Geophys. Res.* 104 (A9), 19859–19869.
- Groves, K.M., Basu, S., Weber, E.J., Smitham, M., Kuenzler, H., Valladares, C.E., Sheehan, R., 1997. Equatorial scintillation and systems support. *Radio Sci.* 32 (5), 2047–2064.
- Gunter, S., 2003. *Satellite Geodesy*. Walter de Gruyter GmbH Co. KG 10785, Berlin, ISBN: 3-11-017549-5, Universitat Hannover Schneiderberg, 50 30167 Hannover, Germany.
- Guochang, X., 2007. *GPS. Theory, Algorithms, and Applications*. Springer-Verlag, Potsdam, Germany.
- Hargreaves, J.K., 1992. *The Solar-Terrestrial Environment*. Cambridge University Press, The Pitt building, Trumpington Street, Cambridge CB2 1RP.
- Hofmann-Wellenhof, B., Lichtenegger, H., Wasle, E., 2007. *Global Navigation Satellite Systems, GPS, GLONASS, Galileo and More*. Springer, Wien, New York, 978-3-211-73012-6.
- Iyer, K.N., Souza, J.R., Pathan, B.M., Abdu, M.A., Jivani, M.N., Joshi, H.P., 2006. A model of equatorial and low latitude VHF scintillation in India. *Indian J. Radio Space Phys.* 35, 98–104.
- Kamide, Y., Maltsev, Y.P., 2007. Geomagnetic storms In: Kamide, Y., Chian, A. (Eds.), *Environment*. Springer-Verlag, Berlin, Heidelberg, pp. 355–374. http://dx.doi.org/10.1007/11367758_14.
- Kelley, M.C., 2009. *The Earth's Ionosphere Plasma Physics and Electrodynamics*, 2nd ed. Academic Press, Elsevier, Cornell University, Ithaca, NY.
- Li, G., Ning, B., Liu, L., Ren, Z., Lei, J., Su, S.Y., 2008. The correlation of longitudinal/seasonal variations of evening equatorial pre-reversal drift and of plasma bubbles. *Ann. Geophys.* 25, 2571–2578.
- Lonchay, M., Cornet, Y., Aquino, M., Warnant, R., 2014. Spatial and stochastic analysis of scintillation data in the frame of absolute GNSS positioning algorithms.

- Geophys. Res. Abstr. 16 (EGU2014-14158).
- Ma, G.Y., Maruyama, T., 2006. A super bubble detected by dense GPS network at East Asian longitudes. *Geophys. Res. Lett.* 33, L21103.
- Melbourne, W.G., Neil, R.E., 1995. Applications of the international GPS service for geodynamics in the next decade. In: Proceedings of the IGS: Special Topics and New Directions, May 15–17. GeoForschungsZentrum, Potsdam, Germany.
- Olwendo, O.J., Baluku, T., Baki, P., Cilliers, P.J., Mito, C., Doherty, P., 2013. Low latitude ionospheric scintillation and zonal irregularity drifts observed with GPS-SCINDA system and closely spaced VHF receivers in Kenya. *Adv. Space Res.* 51, 1715–1726.
- Paznukhov, V.V., Carrano, C.S., Doherty, P.H., Groves, K.M., Caton, R.G., Valladares, C. E., Seemala, G.K., Bridgwood, C.T., Adeniyi, J., Amaesh, L.L.N., Damtie, B., D'ujanga, F.M., Ndeda, J.O.H., Baki, P., Obrou, O.K., Okere, B., Tsidu, G.M., 2012. Equatorial plasma bubbles and L-band scintillations in Africa during solar minimum. *Adv. Space Res.* (30), 675–682.
- Pi, X., Mannucci, A.J., Lindqwister, U.J., Ho, C.M., 1997. Monitoring of global ionospheric irregularities using the worldwide GPS network. *Geophys. Res. Lett.* 24 (18), 2283–2286.
- Scherliess, L., Fejer, B.G., 1999. Radar and satellite global equatorial F region vertical drift model. *J. Geophys. Res.* 104 (4A), 6829–6842.
- Schunk, W.R., Nagy, F.A., 2009. *Ionospheres: Physics, Plasma Physics, and Chemistry*, 2nd ed. Cambridge University press, New York, USA.
- Secan, J.A., Bussey, R.M., Fremouw, E.J., 1995. An improved model of equatorial scintillation. *Radio Sci.* 30 (3), 607–617.
- Seemala, G., Valladares, C., 2011. Statistics of total electron content depletions observed over the South American continent for the year 2008. *Radio Sci.* 46. <http://dx.doi.org/10.1029/2011RS004722>.
- Tanna, H., Karia, S.P., Pathak, K.N., 2013. A study of L band scintillations during the initial phase of rising solar activity at an Indian low latitude station. *Adv. Space Res.* 52, 412–421.
- Valladares, C., Villalobos, J., Sheehan, R., Hagan, M., 2004. Latitudinal extensions of low-latitude scintillations measured with a network of GPS receivers. *Ann. Geophys.* 22 (01), 3155–3175.
- Wanninger, L., 1995. Monitoring ionospheric disturbances using the IGS network. In: Gendt, G., Dick, G. (Eds.), Proceedings of the IGS: Special Topics and New Directions Workshop, May. GeoForschungsZentrum, Potsdam, Germany, p. 57–66.
- Ware, R.H., 1995. The University NAVstar Consortium: global positioning for geosciences research. In: Proceedings of the IGS: Special Topics and New Directions, May 15–17. GeoForschungsZentrum, Potsdam, Germany.
- Zou, Y., Wang, D., 2009. A study of GPS ionospheric scintillations observed at Guilin. *J. Atmos. Sol.-Terr. Phys.* 71, 1948–1958.